Geophysical Research Letters

RESEARCH LETTER
10.1029/2020GL088654

Seafloor Depth of George VI Sound, Antarctic Peninsula, From Inversion of Aerogravity Data

Renata R. Constantino[1], Kirsty J. Tinto[1], Robin E. Bell[1], David F. Porter[1], and Tom A. Jordan[2]

[1]Lamont-Doherty Earth Observatory, Columbia University, Palisades, NY, USA, [2]British Antarctic Survey Cambridge, UK

Key Points:
- We present an improved resolution of bathymetry over George VI Sound from airborne gravity inversion
- New crustal density model across the Sound allows relocation of a major fault and reveals a dense body on the Palmer Land side of the Sound
- A newly identified ridge appears to act as a constriction to ocean circulation between the southern and northern segments of the Sound

Supporting Information:
- Supporting Information S1
- Data Set S1

Correspondence to:
R. R. Constantino,
constantino@ldeo.columbia.edu

Citation:
Constantino, R. R., Tinto, K. J., Bell, R. E., Porter, D. F., & Jordan, T. A. (2020). Seafloor depth of George VI Sound, Antarctic Peninsula, from inversion of aerogravity data. *Geophysical Research Letters*, *47*, e2020GL088654. https://doi.org/10.1029/2020GL088654

Received 29 APR 2020
Accepted 21 AUG 2020
Accepted article online 13 OCT 2020

Abstract George VI Sound is an ~600 km-long curvilinear channel on the west coast of the southern Antarctic Peninsula separating Alexander Island from Palmer Land. The Sound is a geologically complex region presently covered by the George VI Ice Shelf. Here we model the bathymetry using aerogravity data. Our model is constrained by water depths from seismic measurements. We present a crustal density model for the region, propose a relocation for a major fault in the Sound, and reveal a dense body, ~200 km long, flanking the Palmer Land side. The southern half of the Sound consists of two distinct basins ~1,100 m deep, separated by a −650 m-deep ridge. This constricting ridge presents a potential barrier to ocean circulation beneath the ice shelf and may account for observed differences in temperature-salinity (T-S) profiles.

Plain Language Summary Knowing the seafloor depth beneath ice shelves is crucial for understanding the interaction between the ocean and the overlying ice, as the shape of the sea floor influences water circulation pathways. We present a new bathymetric model of the seafloor beneath George VI Ice Shelf on the Antarctica Peninsula. The data for our model were collected from airborne surveys, including the ice surface elevation, ice thickness, and gravity field measurements. We first present a new geological model of the Sound and use our improved data coverage to relocate a previously interpreted geological fault. The new bathymetry model shows that in the southern segment of the Sound, an area with shallow bathymetry and deep ice might be acting as a barrier to the water flow. This information can change our understanding of the circulation between the northern and southern segments of the Sound and can be used in models of how this impacts the melt in the base of the ice shelf.

1. Introduction

The George VI Sound is a channel on the west coast of the southern Antarctic Peninsula separating Alexander Island from Palmer Land (Bell & King, 1998) (Figure 1). The Sound is covered by an ice shelf that is thinner in the north (<250 m) and thicker (up 500 m) in the south (Griggs & Bamber, 2011). The majority of the ice flow (96–97%) feeding the George VI Ice Shelf comes from glaciers on Western Palmer Land (Jenkins & Jacobs, 2008), which are currently experiencing the greatest mass loss from the Antarctic Peninsula (Gourmelen et al., 2019), contributing ~0.1 mm/a to global sea level rise in the last 2 decades (Schannwell et al., 2018). The ice shelf has two ice fronts, both within confined embayments of the Bellingshausen Sea, where Circumpolar Deep Water (CDW) floods the continental shelf (Talbot, 1988). Due to the presence of CDW, the water temperatures near the ice shelf base at both ice fronts exceed 1 °C (Jenkins & Jacobs, 2008).

High basal melt rates around Antarctica have been interpreted as responses to variations in oceanic temperature and circulation (e.g., Holland et al., 2008; Jacobs et al., 2011). Over George VI Ice Shelf, estimated basal melt rates range from 2.8 m/a (Corr et al., 2002) to 6.0 m/a (Dinniman et al., 2012) with a recent study reporting ~4 m/a over a 23 year period (Adusumilli et al., 2018). Future changes in basal melt depend on changes in ocean temperature as well as subsurface currents, steered by the cavity shape, highlighting the importance of accurate bathymetry data for future predictions (e.g., De Rydt et al., 2014; Dutrieux et al., 2014; Goldberg et al., 2019; Rosier et al., 2018).

Bathymetry is one of the outstanding unknowns in understanding the interactions between ocean and ice beneath ice shelves (e.g., Millan et al., 2017; Nitsche et al., 2007; Tinto et al., 2015). Knowledge of the

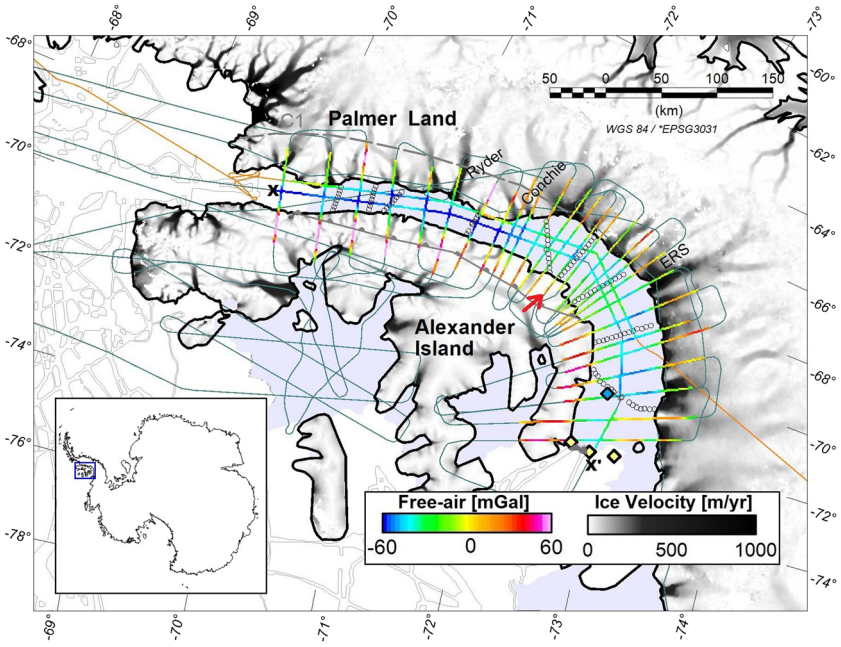

Figure 1. Free-air gravity anomaly from airborne gravity surveys. Grounded ice flow (Mouginot et al., 2017). Floating ice (Fretwell et al., 2013) in light lilac. Flight tracks are represented as green lines (OIB) and orange line (ITGC). Seismic shots (Maslanyj, 1987) shown as white circles, and CTD stations are indicated by yellow (Giulivi & Jacobs, 1997) and blue (Kimura et al., 2015) diamonds. The Ryder, Conchie and ERS glaciers are also shown. The along-axis tie line (Figure 2a) is marked as x-x′, and the crossing line (Figure 2b) is indicated by the red arrow. Tracklines for available bathymetry outboard from ice-shelf is shown as gray contours (Arndt et al., 2013). Part of this data product included in our final grid is highlighted in gray near to x′.

bathymetry beneath the George VI Ice Shelf is essential for modeling ice-ocean interactions and predicting future changes in the glacial mass balance of the Antarctic Peninsula. Previously, the regional bathymetry was based on interpolation of sparse seismic constraints along profiles 20 to 70 km apart (Maslanyj, 1987). Here, we present a new bathymetric model obtained from a high-resolution aerogravity inversion constrained by the seismic depths. Using gravity anomalies to improve the resolution of subice shelf bathymetry can bring new insights into local tectonic evolution of George VI Sound and the regional geological knowledge.

1.1. Geological Setting

The Sound is divided into two morphological segments. The narrow northern segment is between 20 and 35 km wide and trends NNW-SSE. The southern segment is ~60 to 90 km wide and trends SW (Crabtree et al., 1985).

Evidence from geomorphology, radio echo-sounding data, and seismic surveys suggests that the George VI Sound is a tectonic feature (Crabtree et al., 1985; Doake, 1984; King, 1964; Maslanyj, 1988) possibly related to Cenozoic (Storey & Nell, 1988) extension in the West Antarctic Rift System (Eagles et al., 2009). Although the extent of the George VI rift remains uncertain, two major N-S trending fault zones in Palmer Land were inferred from radar and satellite images by Crabtree et al. (1985), with the western fault (C1; Figure 1) interpreted as the eastern boundary of the rift system (Maslanyj, 1987). The western boundary is delimited by the LeMay Fault on Alexander Island (Edwards, 1979) (Figure 1).

The eastern side of the Sound comprises Cretaceous arc-related volcanic and magmatic rocks while the western side is divided into two domains: the Lemay Group (LMG), a Mesozoic accretionary complex (Burn, 1984), and the Fossil Bluff Formation (FBF), composed of Early Cretaceous fore-arc basin sedimentary rocks (Crame & Howlett, 1988).

2. Data Set

2.1. Gravity Anomalies

Between 2009 and 2019, the NASA Operation IceBridge Mission (OIB) collected airborne remote sensing measurements over Earth's polar regions. For this study, we use data that were collected over the Sound from four flights during the 2011 and 2016 campaigns. These flights were flown at a height of ~500 m above the surface at an average speed of 275 kn (142 m/s). The majority of gravity measurements used here were obtained with the Sander Geophysics AIRGrav airborne gravity system. A 70 s temporal filter was applied to the data resulting in a filter half-wavelength of ~5 km (Cochran & Bell, 2012).

An additional along-Sound gravity profile was obtained with the British Antarctic Survey (BAS) Twin Otter in February 2019 as a part of the International Thwaites Glacier Collaboration (ITGC) aerogeophysical survey (Jordan, Porter, et al., 2020). This longitudinal profile (Figure 1) was flown approximately 10 km east of the OIB along-axis tie line. The ITGC free-air anomalies were obtained from a strapdown gravity meter, with an uncertainty of 1.56 mGal, resolving wavelengths of 5 km (Jordan, Robinson, et al., 2020). Crossovers between ITGC anomaly and OIB profiles are 2.8 mGal.

2.2. Bathymetry Constraints

The ice surface elevation is measured with an accuracy of ~10 cm using the Airborne Topographic Mapper (ATM) lidar (Krabill et al., 2002). The ice thickness is measured by the Multi-channel Coherent Radar Depth Sounder (MCoRDS) with approximately 10 m accuracy (Leuschen, 2012).

Nine seismic profiles from Maslanyj (1987) are used to constrain the bathymetry model (Figure 1). The seismic survey was carried out in the 1984–1985 field season along profiles oriented perpendicular to the walls of the Sound, with seismic shots every 3 km along the northern profiles and every 4 km in the south. Profiles were between 20 and 70 km apart and were seldom coincident with flight lines. CTD depths (Giulivi & Jacobs, 1997; Kimura et al., 2015) are also used (Figure S1 in the supporting information).

3. Methods

3.1. Gravity Inversion

Developing the bathymetry model for George VI Sound required three main steps, tie line modeling constrained by seismic depths, cross-sound models pinned to the tie line, and validation. First an initial forward model for the along-axis tie line was developed (x-x′, Figure 1), constrained by the seismically derived depths where available. In the tie line, densities were assigned to the initial model to match the calculated gravity anomaly to the observed gravity anomaly where depths were known. Second, forward models were built for the crossing profiles, with depth constraints from the tie line bathymetry and topographic elevations from the radar measurements over grounded regions. Here we assigned the density along the edge of the Sound based on the available topographic constrains and geological interpretation, and then we inverted for bathymetry within the Sound. Finally, we validated the model by calculating the difference between an interpolation of the gravity-inverted bathymetry and the seismic points that were not used as constraints in the inversion but were included in the final bathymetry model.

In detail, for the tie line (x-x′, Figure 1), ice surface and base were defined by the ATM lidar and by the MCoRDs radar. A density of 0.915 g/cm^3 was assigned to the ice shelf (Doake, 1984), and 1.03 g/cm^3 was assigned to water column. The preliminary crustal configuration was based on the literature. Crabtree et al. (1985) suggest from magnetic anomalies that the Sound is entirely floored by sedimentary rock but does not give constraints on thickness and density. The presence of ~2 km sediments with low density (2.2 g/cm^3) is interpreted by Maslanyj (1988) for the southern portion of the Sound. To approximate sedimentary fill, our model includes a package between seafloor and 2 km depth with a density of 2.4 g/cm^3. Based on isostatic models from Garrett (1990), horizontal interfaces were assumed for the transition from the upper crust (2.7 g/cm^3) to lower crust (2.9 g/cm^3) at 17 km, and from lower crust to mantle (3.2 g/cm^3) at 24 km. Where the tie line intersects seismic profiles, the depth of the seafloor is set equal to the seismically derived depth. In between the seismic depth constraints, the gravity was inverted for bathymetry until the calculated and observed gravity anomalies matched to better than 1 mGal. Here we identified large-scale offset interpreted as denser crust of underlying the sediments in the southern part of the Sound (Figures 2b and 3b).

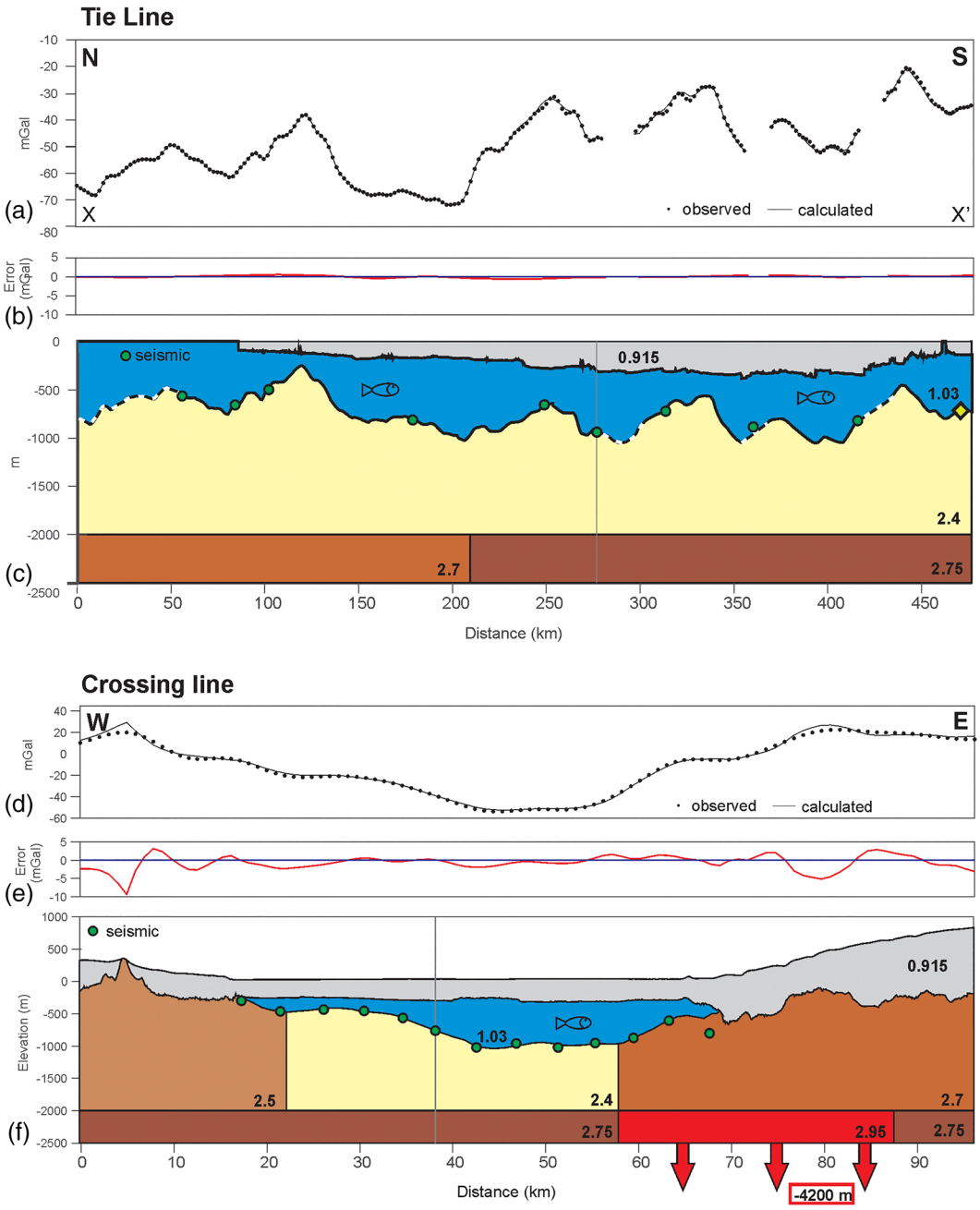

Figure 2. Along-axis tie line and a crossing profile. Observed and calculated anomalies (a, c). Residual gravity anomaly (observed minus modeled) (b, d). Geometry of inverted bathymetry and crustal blocks (e, f). Green dots represent nearby seismic depths projected onto the gravity profile. Gray line marks where profiles intersect. Bathymetry dotted in white represents areas where uncertainty is higher. Red arrows represent the extension of the denser block to a depth of −4.2 km. Profiles are at different scales.

In our second step, where we modeled the crossing profiles, the density configuration was initially set to the tie line densities. The depth where the tie line intersects each crossing profile was set to match the inverted tie lie bathymetry. A long-wavelength trend (~40 mGal over 60 km) was observed in the residuals of the crossing profiles. To account for this regional trend, we modeled the lower crust dipping down toward the Peninsula (compatible with Garrett, 1990) in the crossing lines on the broader, southern part of the Sound (Figure S2).

All the crossing line models were pinned where they intersect the tie line (Figure S1), so that a DC shift (i.e., constant value added or subtracted to the observed gravity, e.g., Holom & Oldow, 2007) is applied to

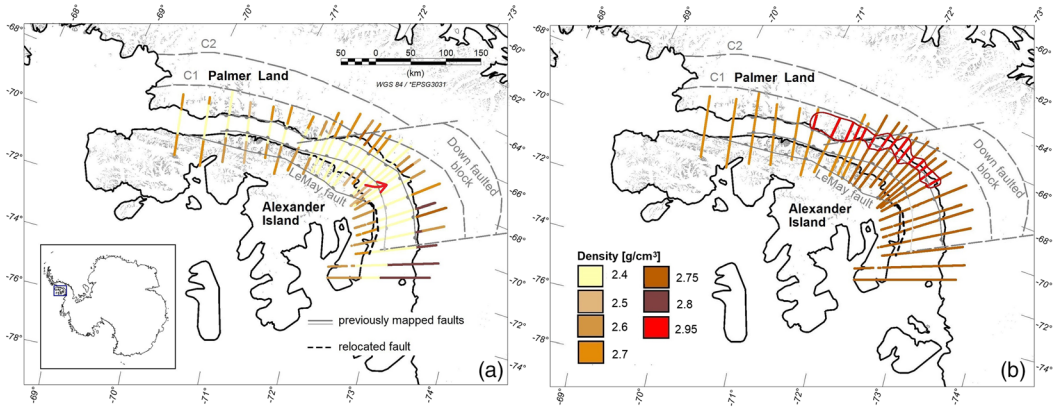

Figure 3. Density distribution in depth. (a) Density from sea level to 2 km depth. (b) Density from 2 to 4.2 km depth. Rock exposures from ATA SCAR GeoMAP v.201907 in gray. Geometry of proposed denser block marked by dark red line. Constricting ridge pointed by the red arrow.

the observed gravity to force the residual between observed and predicted gravity to be zero. The density of the 2 km-deep block at each end of the profiles, where bed elevation is known from radar, was assigned in order to minimize the residuals, before the bathymetry inversion was performed. A residual between the observed and calculated anomaly of up to 20 mGal was observed on the Palmer land side of some profiles, implying the presence of a denser structure of 2.95 g/cm^3 that is discussed in the results.

An initial inversion for bathymetry was performed on the crossing lines. The inversion was performed only where ice is floating. We identified the grounding line along each profile with radar ice thickness and surface altimetry assuming hydrostatic equilibrium. For profiles where the preliminary modeled bathymetry was shallower than the ice base, the geologic model was refined by changing the density of the 2 km-deep subseafloor block in order to account for the excess mass and a new bathymetry inversion performed (Figure 2).

3.2. Uncertainty of the Method

Uncertainty due to the gravimeter accuracy is estimated by calculating the standard deviation (SD) of the differences between gravity measurements at the crossover points between lines, which is 2.4 mGal. To quantify this value in meters, a simple Bouguer slab correction is applied to the residual considering a density contrast of 1,670 kg/cm^3 between rock and water, which gives a value of ± 34 m.

The uncertainty due to the pinning point constraining the inversion is the uncertainty of the seismic measurements, established by Maslanyj (1987) to be between ±5 and ±10 m. The uncertainty from variations in geology is estimated by the SD of the gravity residuals where topography is known from radar and residuals must be due to density variations. The SD of 6.3 mGal is equivalent to ±89 m of bathymetry. This gives a total uncertainty of the bathymetry model of ±133 m, similar to the error estimated from other subice shelf bathymetry studies (e.g., Tinto et al., 2015, 160 m; Boghosian et al., 2015, 110 m; Jordan, Porter, et al., 2020, 100 m).

4. Results

No systematic difference in water depth is seen between the seismic points in the northern and southern sections of the Sound along the tie line (Figure 2a), but a clear difference is observed in the gravity signal. Gravity anomalies range from approximately −70 to −40 mGal in the northern part, and approximately −50 to −20 mGal in the southern part. We have modeled this variation as being due to a denser upper crust (2.75 g/cm^3) in the southern half of the Sound. The ITGC line (Figure 1) was treated the same way as the tie line, and the inverted bathymetry was then compared to the crossing profiles with a SD of ~69 m.

We have identified density variations within the crust from the forward models and accounted for them (Figure 3) to best match the observed and calculated anomalies where bed elevation and bathymetry are constrained. No inversion was performed to obtain densities. The upper layer of rock extends to a depth of 2.0 km (Figure 3a). Within the Sound, this layer is assigned a density of 2.4 g/cm^3, and depth is constrained by the seismic surveys where they intersect the tie line. At the edges of the profiles, gravity residuals over

grounded ice indicate denser material. The boundary between units is marked by the maximum gradient of the gravity anomaly in the area that the density contrast must occur. With no constraints on the shape of these boundaries, they were defined as simple vertical structures (Figure 2b). Between 2.0 and 4.2 km depth, the density of 2.7 g/cm^3 was assigned for the northern profiles and 2.75 g/cm^3 for the southern profiles, consistent with the tie line regional structure. A block of denser material (2.95 g/cm^3) is identified in the central profiles on the Palmer Land side (Figure 3b). The boundary of the dense body within the Sound is identified by the location of an increased gradient in the gravity field that can be traced on multiple adjacent survey lines. The seismic profile shown on Figure 2b demonstrates that this gradient increase (~58 km along profile) is not due to the bathymetry and is caused by dense material beneath the surface.

Our final bathymetry model for the George VI Sound includes all bathymetry constraints (Figure 1), and the data were gridded using minimum curvature with a cell size of 1 km. The final grid (Figure 4a) reveals shallower water depths for the northern segment (generally <1,000 m) compared to the south (up to 1,263 m). Bathymetry shoals at the sides and deepens toward the center of the Sound. The southern front of the ice shelf is underlain by a narrow, deep trough that extends ~50 km from the ice front and widens beneath the ice shelf. Our results show that the broad southern basin that underlies the ice shelf is divided into two distinct subbasins, separated by a shallow ridge, which we refer to as the constricting ridge. The water column thickness (Figure 4c) estimated from our bathymetry model and the radar ice base measurements (Figure S16) shows a significant thinning to less than 150 m between the two deeper southern basins. This thin water column, resulting both from the thick ice and the shallow ridge, represents a potential barrier to circulation within the southern limb of the Sound. This, combined with thick ice and shallow bathymetry, may be more restrictive to ocean circulation than the narrowing between the northern and southern sections of the Sound. To highlight the increased resolution offered by the new data and particularly over this shallow ridge, we show a comparison between our final gridded bathymetry with Bedmap2 and Bedmachine in Figures 17 and 18).

4.1. Validating the Model

The majority of seismic shots (Maslanyj, 1987) are not colocated with the gravity profiles and were not used in the inversion. We tested the accuracy of the gravity model by gridding the bathymetry from just the inverted profiles and calculating the difference between this grid and the seismic depths and found a SD of ~100 m. We did the same comparison for Bedmap2 (Fretwell et al., 2013) and Bedmachine (Morlighem et al., 2020), and SDs of 97 and 96 m were found, respectively. When we compare the seismic depths to our final grid (Figure 4a), which includes all available depth constraints, the differences are much smaller, and the SD is ~14 m. These differences are plotted (Figures S3 to S15), and data for each seismic shot can be accessed on Data Set S1.

The cross sound profile shown in Figure 2d illustrates the seismic depths projected onto the model profile, which are generally in excellent agreement. The exception is the easternmost shot. To match the inverted seafloor with the seismic depth at the outlying point, the predicted gravity would be lower than the observed. The seismic shot may be in the center of a glacial trough carved out by the incoming glacier, while the gravity data, offset 5 km from the seismic survey, clips the shoulder of this steep trough. This discrepancy could also be related to unaccounted subsurface density variations.

5. Discussion

5.1. Geological Interpretation

Geological bodies included in the models (Figure 3) are presented as simplified blocks that minimize the residuals between observed and predicted gravity over grounded ice. The density boundaries on the shallow structure (Figure 3a) suggest that in the southern Sound the western fault is closer to the coast than the fault inferred from Bell and King (1998) and may link with the onshore LeMay fault. The eastern edge of the Sound is very well aligned with the margin of the deeper dense structure (Figure 3b).

The modeled density of the constricting ridge material is the same as that of sedimentary rock and the rest of the floor of the Sound (2.4 g/cm^3). This density supports its interpretation as a bathymetric feature. The ridge may either be a feature carved from the FBF or a deposit of material eroded off Palmer Land by the ERS glacier.

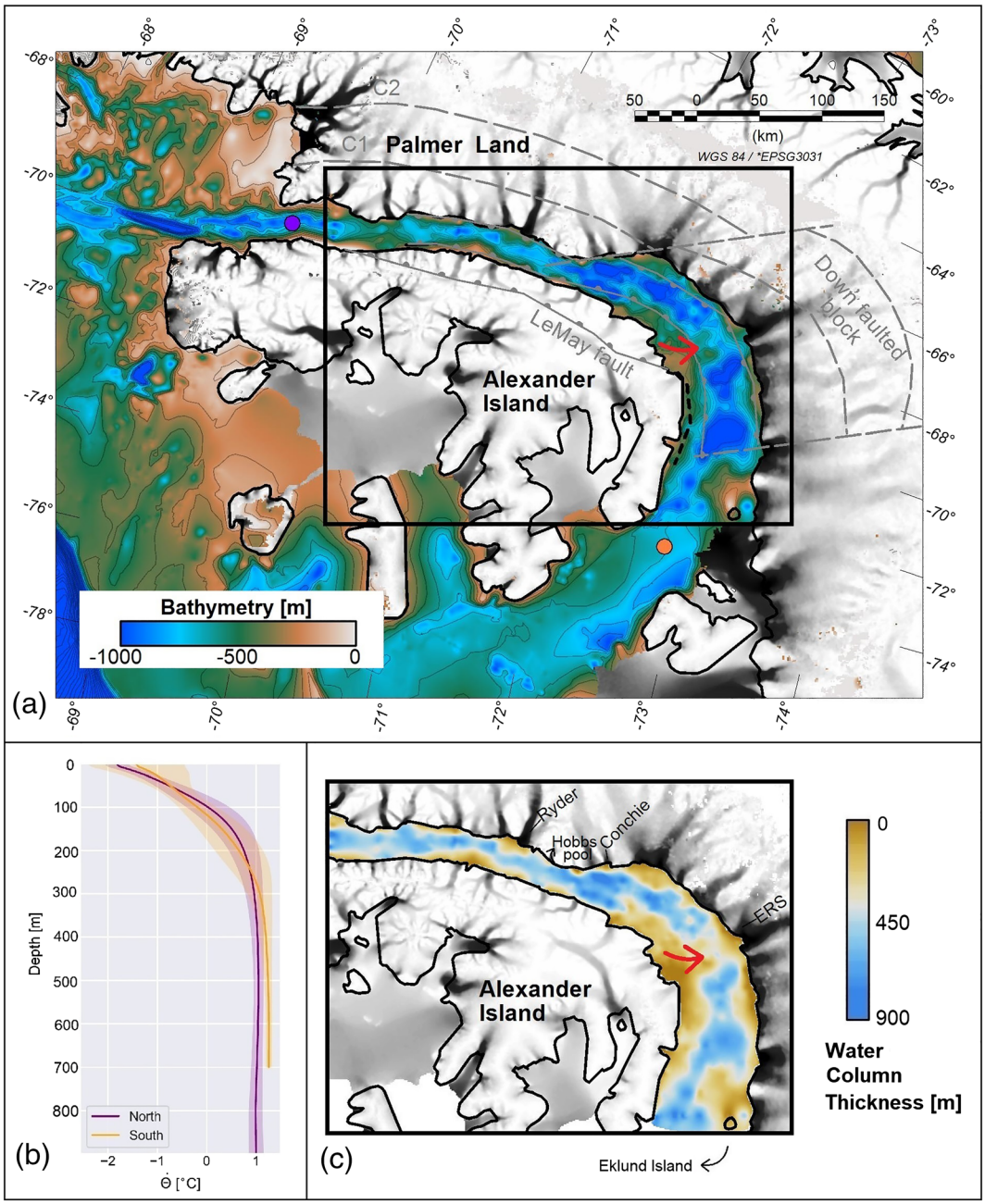

Figure 4. (a) George VI Sound bathymetry. Outside the black box, bathymetry from Bedmap2. Location of plots on panel b represented by the purple and orange circles. Constricting ridge pointed by the red arrow (b) SOSE (Mazloff et al., 2010) potential temperatures (2008–2012) for Northern and Southern Sound entrances. Mean (solid line) and STD (shaded). (c) Water column thickness.

A magnetic body (Jones & Maslanyj, 1987) probably composed of volcanic and plutonic rocks of the Mesozoic Arc (Bell & King, 1998) with its western boundary being limited by the fault along the eastern edge of the Sound might correspond to our modeled dense body. This magnetic anomaly is interpreted to be the expression of a more mafic arc forming the western half of Palmer Land (Ferraccioli et al., 2006), consistent with the presence of higher density material in this region. Here we propose that the dense body underlies the eastern border of George VI Sound and extends to western Palmer Land (Figure 3b). The denser structure is offset by the fault interpreted by Bell and King (1998) (Figure 3b), suggesting that the high-density body was emplaced before the fault motion initiated. In addition, the offset of the dense body is consistent with

a component of left-lateral offset along this proposed fault system. The Antarctic Peninsula displays widespread evidence for left-lateral faulting along a similar trend (340°) to our proposed fault's trend (330°). This is well dated to the Palmer Land Event in Albian times (e.g., Vaughan et al., 2012) and so both comfortably postdates the Lower Cretaceous timing of the mafic arc (Ferraccioli et al., 2006) and predates the right-lateral opening of George VI Sound in Cenozoic times. The proposed offsetting fault system coincides with the change in midcrustal density revealed along the tie-line model, suggesting that it may be a significant crustal scale feature. The southern and northern limits of this structure might indicate the presence of additional bordering SW-NW faults.

The Sound has different magnetic characteristics along its extent, with a low amplitude variation magnetic field with mainly negative anomalies in the northern and high amplitude variation magnetic field with positive anomalies in the southern section (Maslanyj, 1988). The proposed denser body is located between these two regions. The change in magnetic signature between the southern and northern parts of the Sound (Golynsky et al., 2018; Figure S19) corresponds to the location of the change in basement density along the length of the tie line (Figure 2b), indicating the change in basement material.

5.2. Bathymetry Implications on Deep Water Pathways

A circulation model for the northern segment of George VI driven primarily by the basal melting process was proposed by Potter and Paren (1985). Ice shelf basal melt becomes fresher and positively buoyant, upwelling toward the shallower Northern ice front while drawing up warm CDW that had been advected under the ice shelf at depth. They found this glacial meltwater collecting in a northward outflow at the northern entrance, enhanced in the west by Coriolis force.

Based on temperature-salinity (T-S) profiles along the length of the Sound, Potter and Paren (1985) proposed that this circulation in the north did not extend all the way to the southern ice front, hypothesizing a constriction somewhere between Eklund Islands and Hobbs pool (Figure 4c) possibly by a thick ice keel extending across the Sound. The newly discovered constricting ridge is beneath thick ice imaged by radar sounding (Figure 2c) outboard from the ERS Glacier (Figure 4c) and results in the thinnest across-sound water column beneath the ice shelf (highlighted in Figure 4c). This thin water cavity will restrict the pathways of deep CDW inflow (Holland et al., 2010; Jenkins & Jacobs, 2008) affecting along-Sound flow, potentially leading to the disparate patterns of modern day basal melting evident in satellite observations between the northern and southern sections of the Sound (Adusumilli et al., 2018).

5.3. Oceanographic Setting of Enhanced Basal Melt Rates

These results allow for new interpretations of how and where the thermocline strength and depth can drive basal melting of the peninsular ice shelf. Model outputs from the adjoint ocean model SOSE (Mazloff et al., 2010) show warmest temperatures below the thermocline at ~200 m deep on the George VI northern ice front where the CDW advects from Marguerite Bay beneath the ice shelf (Holt et al., 2013), while it is below ~300 m on the southern ice front (Figure 4c) where the deep water flows northward under the ice shelf from the Ronne Entrance (Jenkins & Jacobs, 2008). The greater thermal forcing (difference between in situ temperature and the pressure-dependent freezing point of seawater) in the southern part of the ice shelf means that ice below the thermocline, there is more susceptible to basal melting. Glaciers and ice streams that feed into the Southern ice shelf are predominantly grounded deeper than 300 m below sea level, coinciding with locations of higher basal melt rates (Adusumilli et al., 2018), and agreeing with velocity speedup of the deepest glaciers on the Palmer Land coast (Hogg et al., 2017). In the northern segment, with the exception of deep-grounded Ryder and Conchie glaciers (Figure 4c), most ice shelf ice in the Northern Sound is shallower than the thermocline and therefore is less susceptible to melting by this deep heat source.

6. Conclusion

We present a new bathymetry model for the George VI Sound using airborne gravity data. The seafloor under the ice shelf is an essential boundary condition for modeling ice-ocean interactions and projections of ice changes along the Antarctic Peninsula. We have modeled the density structure of the Sound and have defined the extent of a previously proposed suite of volcanic and plutonic rocks faulted by subsequent tectonic activity. We have relocated a previously inferred fault in the Sound based on modeled density variations. Deep bathymetry, where ice is grounded below the thermocline on the eastern side of the Sound,

corresponds to fast ice flow areas that are potential spots for high basal melt rates. In the southern section of the Sound, a significant across-sound ridge is proposed as a constricting barrier between the southern and northern circulation. The new model has a higher resolution than previously available, crucial for ocean circulation models used for investigating CDW pathways and associated heat transport, a major driver of ice shelf melt, and ice sheet mass changes.

Data Availability Statement

ITGC data were acquired as part of the British Antarctic Survey (BAS) National Capability contribution to the International Thwaites Glacier 360 Collaboration (ITGC). Data from Operation IceBridge are available from the National Snow and Ice Data Center (at http://nsidc.org/data/icebridge). Bathymetry model data from Operation IceBridge are archived at the National Snow and Ice Data Center (NSDISC) as data products IGBTH3 and IGBTH4. See https://nsidc.org/data/igbth3 and https://nsidc.org/data/igbth4. Data for bathymetry model is available online (at https://pgg.ldeo.columbia.edu/data/operation-icebridge).

Acknowledgments
This work was funded by NSF 1842064 and NASA NNX16AJ65G. We thank Stan Jacobs, Fernando Paolo, and Pierre Dutrieux for discussion contributions. We also thank Katrina Zamudio and Journey Berry for their work contribution.

References

Adusumilli, S., Fricker, H. A., Siegfried, M. R., Padman, L., Paolo, F. S., & Ligtenberg, S. R. (2018). Variable basal melt rates of Antarctic Peninsula ice shelves, 1994–2016. *Geophysical Research Letters*, *45*, 4086–4095. https://doi.org/10.1002/2017GL076652

Arndt, J. E., Schenke, H. W., Jakobsson, M., Nitsche, F. O., Buys, G., Goleby, B., et al. (2013). The International Bathymetric Chart of the Southern Ocean (IBCSO) Version 1.0—A new bathymetric compilation covering circum-Antarctic waters. *Geophysical Research Letters*, *40*, 3111–3117. https://doi.org/10.1002/grl.50413

Bell, A. C., & King, E. C. (1998). New seismic data support Cenozoic rifting in George VI Sound, Antarctic Peninsula. *Geophysical Journal International*, *134*(3), 889–902. https://doi.org/10.1046/j.1365-246x.1998.00605.x

Boghosian, A., Tinto, K., Cochran, J. R., Porter, D., Elieff, S., Burton, B. L., & Bell, R. E. (2015). Resolving bathymetry from airborne gravity along Greenland fjords. *Journal of Geophysical Research: Solid Earth*, *120*, 8516–8533. https://doi.org/10.1002/2015JB012129

Burn, R. W. (1984). *The geology of the LeMay Group, Alexander Island* (Vol. 109). British Antarctic Survey.

Cochran, J. R., & Bell, R. E. (2012). Inversion of IceBridge gravity data for continental shelf bathymetry beneath the Larsen Ice Shelf, Antarctica. *Journal of Glaciology*, *58*(209), 540–552. https://doi.org/10.3189/2012JoG11J033

Corr, H. F., Jenkins, A., Nicholls, K. W., & Doake, C. S. M. (2002). Precise measurement of changes in ice-shelf thickness by phase-sensitive radar to determine basal melt rates. *Geophysical Research Letters*, *29*(8), 1232. https://doi.org/10.1029/2001GL014618

Crabtree, R. D., Storey, B. C., & Doake, C. S. M. (1985). The structural evolution of George VI Sound, Antarctic Peninsula. *Tectonophysics*, *114*(1–4), 431–442. https://doi.org/10.1016/0040-1951(85)90025-3

Crame, J. A., & Howlett, P. J. (1988). Late Jurassic and Early Cretaceous biostratigraphy of the Fossil Bluff Formation, Alexander Islands. *British Antarctic Survey Bulletin*, *78*, 1–35.

De Rydt, J., Holland, P. R., Dutrieux, P., & Jenkins, A. (2014). Geometric and oceanographic controls on melting beneath Pine Island Glacier. *Journal of Geophysical Research: Oceans*, *119*, 2420–2438. https://doi.org/10.1002/2013JC009513

Dinniman, M. S., Klinck, J. M., & Hofmann, E. E. (2012). Sensitivity of circumpolar deep water transport and ice shelf basal melt along the West Antarctic Peninsula to changes in the winds. *Journal of Climate*, *25*(14), 4799–4816. https://doi.org/10.1175/JCLI-D-11-00307.1

Doake, C. S. M. (1984). Ice-shelf densities from a comparison of radio echo and seismic soundings. *Annals of Glaciology*, *5*, 47–50. https://doi.org/10.3189/1984AoG5-1-47-50

Dutrieux, P., de Rydt, J., Jenkins, A., Holland, P. R., Ha, H. K., Lee, S. H., et al. (2014). Strong sensitivity of Pine Island ice-shelf melting to climatic variability. *Science*, *343*(6167), 174–178. https://doi.org/10.1126/science.1244341

Eagles, G., Larter, R. D., Gohl, K., & Vaughan, A. P. (2009). West Antarctic rift system in the Antarctic Peninsula. *Geophysical Research Letters*, *36*, L21305. https://doi.org/10.1029/2009GL040721

Edwards, C. W. (1979). New evidence of major faulting on Alexander Island. *British Antarctic Survey Bulletin*, *49*, 15–20.

Ferraccioli, F., Jones, P. C., Vaughan, A. P. M., & Leat, P. T. (2006). New aerogeophysical view of the Antarctic Peninsula: More pieces, less puzzle. *Geophysical Research Letters*, *33*, L05310. https://doi.org/10.1029/2005GL024636

Fretwell, P., Pritchard, H. D., Vaughan, D. G., Bamber, J. L., Barrand, N. E., Bell, R., et al. (2013). Bedmap2: Improved ice bed, surface and thickness datasets for Antarctica. *The Cryosphere*, *7*(1), 375–393. https://doi.org/10.5194/tc-7-375-2013

Garrett, S. W. (1990). Interpretation of reconnaissance gravity and aeromagnetic surveys of the Antarctic Peninsula. *Journal of Geophysical Research*, *95*(B5), 6759–6777. https://doi.org/10.1029/JB095iB05p06759

Giulivi, C. F., & Jacobs, S. S. (1997). Oceanographic data in the Amundsen and Bellingshausen Seas: NB Palmer cruise 9402, February–March 1994. Lamont-Doherty Earth Observatory Tech. Rep, 97–93.

Goldberg, D. N., Gourmelen, N., Kimura, S., Millan, R., & Snow, K. (2019). How accurately should we model ice shelf melt rates? *Geophysical Research Letters*, *46*, 189–199. https://doi.org/10.1029/2018GL080383

Golynsky, A. V., Ferraccioli, F., Hong, J. K., Golynsky, D. A., von Frese, R. R. B., Young, D. A., et al. (2018). New magnetic anomaly map of the Antarctic. *Geophysical Research Letters*, *45*, 6437–6449. https://doi.org/10.1029/2018GL078153

Gourmelen, N., Dow, C. F., Goldberg, D., & Morlighem, M. (2019). Heterogeneous basal melt rates under George VI Ice Shelf, Antarctic Peninsula. In *AGU Fall Meeting 2019*. AGU.

Griggs, J. A., & Bamber, J. L. (2011). Antarctic ice-shelf thickness from satellite radar altimetry. *Journal of Glaciology*, *57*(203), 485–498. https://doi.org/10.3189/002214311796905659

Hogg, A. E., Shepherd, A., Cornford, S. L., Briggs, K. H., Gourmelen, N., Graham, J. A., et al. (2017). Increased ice flow in Western Palmer Land linked to ocean melting. *Geophysical Research Letters*, *44*, 4159–4167. https://doi.org/10.1002/2016GL072110

Holland, P. R., Jenkins, A., & Holland, D. M. (2008). The response of ice shelf basal melting to variations in ocean temperature. *Journal of Climate*, *21*(11), 2558–2572.

Holland, P. R., Jenkins, A., & Holland, D. M. (2010). Ice and ocean processes in the Bellingshausen Sea, Antarctica. *Journal of Geophysical Research*, *115*, C05020. https://doi.org/10.1029/2008JC005219

Holom, D. I., & Oldow, J. S. (2007). Gravity reduction spreadsheet to calculate the Bouguer anomaly using standardized methods and constants. *Geosphere*, *3*(2), 86–90. https://doi.org/10.1130/GES00060.1

Holt, T. O., Glasser, N. F., Quincey, D. J., & Siegfried, M. R. (2013). Speedup and fracturing of George VI Ice Shelf, Antarctic Peninsula. *Cryosphere Discussions*, *7*(1), 373–417. https://doi.org/10.5194/tcd-7-373-2013

Jacobs, S. S., Jenkins, A., Giulivi, C. F., & Dutrieux, P. (2011). Stronger ocean circulation and increased melting under Pine Island Glacier ice shelf. *Nature Geoscience*, *4*(8), 519–523. https://doi.org/10.1038/NGEO1188

Jenkins, A., & Jacobs, S. (2008). Circulation and melting beneath George VI ice shelf, Antarctica. *Journal of Geophysical Research*, *113*, C04013. https://doi.org/10.1029/2007JC004449

Jones, J. A., & Maslayj, M. P. (1987). *An aeromagnetic study of southern Palmer Land and eastern Ellsworth Land. Proceedings of the Fifth International Symposium on Antarctic Earth Sciences* (pp. 404–409). Cambridge: Cambridge University Press.

Jordan, T., Robinson, C., Porter, D., Locke, C., & Tinto, K. (2020). Processed line aerogravity data over the Thwaites Glacier region (2018/19 season) [data set]. UK Polar Data Centre, Natural Environment Research Council, UK Research & Innovation. https://doi.org/10.5285/B9B28A35-8620-4182-BF9C-638800B6679B

Jordan, T. A., Porter, D., Tinto, K., Millan, R., Muto, A., Hogan, K., et al. (2020). New gravity-derived bathymetry for the Thwaites, Crosson and Dotson ice shelves revealing two ice shelf populations. *The Cryosphere*, *14*(9), 2869–2882. https://doi.org/10.5194/tc-14-2869-2020

Kimura, S., Nicholls, K. W., & Venables, E. (2015). Estimation of ice shelf melt rate in the presence of a thermohaline staircase. *Journal of Physical Oceanography*, *45*(1), 133–148. https://doi.org/10.1175/JPO-D-14-0106.1

King, L. (1964). *Pre-glacial geomorphology of Alexander Island. Antarctic geology* (Vol. 53, p. 64). Amsterdam: North-Holland Publishing Company.

Krabill, W. B., Abdalati, W., Frederick, E. B., Manizade, S. S., Martin, C. F., Sonntag, J. G., et al. (2002). Aircraft laser altimetry measurement of elevation changes of the Greenland ice sheet: Technique and accuracy assessment. *Journal of Geodynamics*, *34*(3–4), 357–376. https://doi.org/10.1016/S0264-3707(02)00040-6

Leuschen, C. (2012). IceBridge MCoRDS L2 Ice Thickness. National Snow and Ice Data Center.

Maslanyj, M. P. (1987). Seismic bedrock depth measurements and the origin of George VI Sound, Antarctic Peninsula. *British Antarctic Survey Bulletin*, *75*, 51–65.

Maslanyj, M. P. (1988). Gravity and aeromagnetic evidence for the crustal structure of George VI Sound, Antarctic Peninsula. *British Antarctic Survey Bulletin*, *79*, 1–16.

Mazloff, M. R., Heimbach, P., & Wunsch, C. (2010). An eddy permitting Southern Ocean state estimate. *Journal of Physical Oceanography*, *40*(5), 880–899. https://doi.org/10.1175/2009JPO4236.1

Millan, R., Rignot, E., Bernier, V., Morlighem, M., & Dutrieux, P. (2017). Bathymetry of the Amundsen sea embayment sector of West Antarctica from operation IceBridge gravity and other data. *Geophysical Research Letters*, *44*, 1360–1368. https://doi.org/10.1002/2016GL072071

Morlighem, M., Rignot, E., Binder, T., Blankenship, D., Drews, R., Eagles, G., et al. (2020). Deep glacial troughs and stabilizing ridges unveiled beneath the margins of the Antarctic ice sheet. *Nature Geoscience*, *13*(2), 132–137. https://doi.org/10.1038/s41561-019-0510-8

Mouginot, J., Scheuchl, B., & Rignot, E. (2017). Updated 2017. MEaSUREs Annual Antarctic Ice Velocity Maps 2005–2017, Version 1. [subset 2016–2017]. Boulder, Colorado USA. NASA National Snow and Ice Data Center Distributed Active Archive Center. https://doi.org/10.5067/9T4EPQXTJYW9. [Date Accessed on February 9th of 2020].

Nitsche, F. O., Jacobs, S. S., Larter, R. D., & Gohl, K. (2007). Bathymetry of the Amundsen Sea continental shelf: Implications for geology, oceanography, and glaciology. *Geochemistry, Geophysics, Geosystems*, *8*, Q10009. https://doi.org/10.1029/2007GC001694

Potter, J. R., & Paren, J. G. (1985). Interaction between ice shelf and ocean in George VI Sound, Antarctica. *Oceanology of the Antarctic Continental Shelf*, *43*, 35–58. https://doi.org/10.1029/AR043p0035

Rosier, S. H., Hofstede, C., Brisbourne, A. M., Hattermann, T., Nicholls, K. W., Davis, P. E. D., et al. (2018). A new bathymetry for the southeastern Filchner-Ronne ice shelf: Implications for modern oceanographic processes and glacial history. *Journal of Geophysical Research: Oceans*, *123*, 4610–4623. https://doi.org/10.1029/2018JC013982

Schannwell, C., Cornford, S., Pollard, D., & Barrand, N. E. (2018). Dynamic response of Antarctic Peninsula Ice Sheet to potential collapse of Larsen C and George VI ice shelves. *The Cryosphere*, *12*(7), 2307–2326. https://doi.org/10.5194/tc-12-2307-2018

Storey, B. C., & Nell, P. A. R. (1988). Role of strike-slip faulting in the tectonic evolution of the Antarctic Peninsula. *Journal of the Geological Society*, *145*(2), 333–337. https://doi.org/10.1144/gsjgs.145.2.0333

Talbot, M. H. (1988). Oceanic environment of George VI ice shelf, Antarctic Peninsula. *Annals of Glaciology*, *11*, 161–164. https://doi.org/10.3189/S0260305500006480

Tinto, K. J., Bell, R. E., Cochran, J. R., & Münchow, A. (2015). Bathymetry in Petermann fjord from operation IceBridge aerogravity. *Earth and Planetary Science Letters*, *422*, 58–66. https://doi.org/10.1016/j.epsl.2015.04.009

Vaughan, A. P., Leat, P. T., Dean, A. A., & Millar, I. L. (2012). Crustal thickening along the West Antarctic Gondwana margin during mid-Cretaceous deformation of the Triassic intra-oceanic Dyer Arc. *Lithos*, *142*, 130–147.